

# Dendritic propagation on circular electrodes: The impact of curvature on the packing density

Asghar Aryanfar<sup>1,\*</sup>, Ali Tayyar<sup>2</sup>, and William A. Goddard, III<sup>3</sup>

<sup>1</sup>*Mechanical Engineering, Bogazici University, Bebek, Istanbul, Turkey 34342*

<sup>2</sup>*Mechanical Engineering, American University of Beirut, Riad El-Solh, Lebanon 1107 2020*

<sup>3</sup>*California Institute of Technology, 1200 E. California Blvd, Pasadena, California 91125, USA*



(Received 11 March 2023; accepted 16 June 2023; published 10 July 2023)

The dendritic growth in rechargeable batteries is one of the hurdles for the utilization of high energy-density elements, such as alkaline metals, as the electrode. Herein we explore the preventive role of the curved electrode surface in the cylindrical electrode design versus the flat geometry on the stochastic evolution of the dendritic crystals. In this regard we establish a coarse-grained Monte Carlo paradigm in the polar coordinates  $(r, \theta)$ , which runs in a larger scale of time and space ( $\sim \mu\text{s}$ ,  $\sim \text{nm}$ ) than those of interionic collisions ( $\sim \text{fs}$ ,  $\text{\AA}$ ). Subsequently we track the density and the maximum reach of the microstructures in real time, and we elaborate on the underlying mechanisms for their correlation of the relative dendrite measure with the electrode curvature. Such quantification of the positive impact of the curvature on suppressing dendrites could be utilized as an effective longevity design parameter, particularly for the cases prone to dendritic propagation.

DOI: [10.1103/PhysRevE.108.014801](https://doi.org/10.1103/PhysRevE.108.014801)

## I. INTRODUCTION

The escalating energy demand during recent decades has necessitated the development of more efficient energy storage systems [1,2]. Among various technologies, batteries have garnered significant attention due to their clean, low-carbon, high energy density. In particular, they have recently been utilized in the wide range of portable electronics, manufacturing, the service industry [3], and the renewable energy sector [4,5]. In this context, lithium-ion batteries have been extensively researched, owing to their high energy density, low self-discharge rate, lack of memory effect, high open-circuit voltage, and long lifespan [6]. The expansion of lithium-ion batteries, with over 5 billion currently in use worldwide, attests to the technological maturity and widespread acceptance of this technology [7], which could be a viable solution for the power interruptions in the United States that result in an annual cost of around \$80 billion [8].

Despite the numerous advancements, the electrochemical degradation of lithium-ion batteries remains a critical concern [9,10]. In particular, the dendritic growth, resulting from the formation of conductive filaments on the lithium electrode, can lead to short circuiting and thermal runaway, which ultimately leads to battery failure [11,12].

The precise mechanism of dendritic growth is not fully understood, but it is widely accepted that it is influenced by various factors such as complexity in the current density [13–15], electrolyte composition [16], and electrode geometry and microscale curvature [17,18] surface defects (i.e., kinks) [19] and interaction with the solid electrolyte interphase [20,21].

Several studies have attempted to improve the resistance to dendritic growth via shielding with alternative compounds

[22], imposing external magnetic fields [23], guiding scaffolds [24], and using 1D nanofiber arrays in the polymer electrolyte [25].

From the physical perspective, the dendritic microstructures can be characterized spatially via porosity [26], tortuosity [27,28], and the MacMullin number [29]. However, a comprehensive understanding of the relationship between electrode geometry and dendritic growth remains elusive. Previous and recent characterization methods include coupling the electrochemical potential to the stress and the formation of microcracks [30,31], phase-field modeling [32,33], and coarse-grained modeling [34,35].

The tendency for dendritic development primarily is due more to nonequilibrium kinetics of ionic transportation and chemical bonding than to the equilibrium-based thermodynamics. The formation of extended branches is due to the higher accessibility of the upcoming ions to the outer asperities rather than the inner voids. Such imbalance is exacerbated additionally due to the formed electric field, which is biased toward the tips.

This paper presents a detailed investigation of the effect of polar and planar configurations of electrode-positing microstructures on dendritic growth. Starting from the translation of Cartesian  $(x, y)$  to polar  $(r, \theta)$  coordinates, we compare the cylindrical and rectangular electrodepositions and determine the density in both media. Our findings provide insights into the critical role of electrode curvature in dendritic growth and pave the way for the development of improved battery designs with enhanced performance and safety.

## II. METHODOLOGY

We tune the geometry as an effective, convenient, and accessible factor in order to increase the tendency of the ions of getting diverted from the growing tips and directed into the inner voids. The formation of the voltage profile and

\*Corresponding author: [aryanfar@caltech.edu](mailto:aryanfar@caltech.edu)

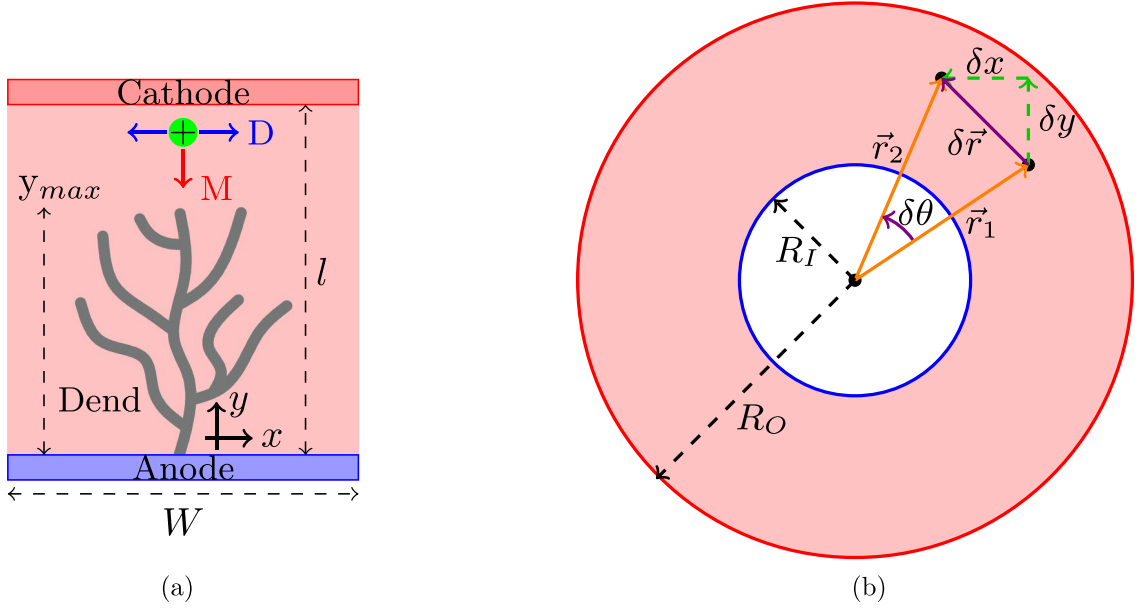


FIG. 1. Parameters of dendritic growth in the planar (a) and polar (b) electrodeposition, which are defined by  $W \times l$  and an intercircular area between the radii of  $R_I$  and  $R_O$  respectively, which pertain to the identical electrodeposition real estates ( $l = 2\pi R_I$ ), the interelectrode distance ( $l = R_O - R_I$ ), and free deposited ions  $N$ . (a) Planar electrodeposition ( $x, y$ ):  $l$ : inter-electrode distance,  $W$ : domain width,  $y_{max}$ : highest dendrite elevation. The vector  $D$  represent the randomness of the diffusion event while the electro-migration vector  $M$  is directed toward tips. (b) Polar characterization ( $r, \theta$ ):  $R_I, R_O$  radii of inner and outer circles.  $\vec{r}_1$  and  $\vec{r}_2$ : the position vector before/ after the displacement.  $\delta \vec{r}$  and  $\delta \theta$ : the change in the radial distance and angle,  $\delta x$  and  $\delta y$ : the horizontal/vertical displacements.

subsequent electric field is a deterministic factor in the ionic movement, particularly the dominant factor in high-voltage and low-concentration applications. In this regard one could calculate the initial electric field for both planar and polar electrode geometries. Based on the Gauss law [36] one has

$$\nabla^2 V = \frac{e(z_a C_a - z_c C_c)}{\epsilon}, \quad (1)$$

where  $V$  is the voltage value,  $z_a, z_c$  and  $C_a$  and  $C_c$  are anionic and cationic valence and concentration, respectively, and  $\epsilon$  is the vacuum permittivity of the electrolytic medium.

### A. Equivalent arrangement

Figures 1(a) and 1(b) illustrate the planar and polar electrode layouts, which are characterized by the dimensions  $W \times l$  and inner and outer radii  $R_I, R_O$ , respectively. In order to define equivalent configurations they should both contain identical properties, to leave out only the impact of curvature. Therefore other than equal interelectrode voltage  $\Delta V$  and number of deposited ions  $N$ , geometry-wise they should both contain identical areal real estate  $A$  for electrodeposition ( $A_{xy} = A_{r\theta}$ ) as well as identical interelectrode distance  $l$  ( $l_{xy} = l_{r\theta}$ ), where the subscripts  $xy$  and  $r\theta$  denote the planar and polar frameworks. Translating these two equations leads to

$$\begin{aligned} A_{xy} = A_{r\theta} &\rightarrow W = 2\pi R_I \\ l_{xy} = l_{r\theta} &\rightarrow l = R_O - R_I. \end{aligned} \quad (2)$$

The radius of the curvature  $R_I$  is typically significantly larger than the interelectrode gap  $l$  ( $R_I \gg l$ ). In order to differentiate between the planar and polar configurations, we

consider the square domain ( $W = l$ ), which leads to

$$\begin{aligned} R_I &= \frac{l}{2\pi} \\ R_O &= (1 + 2\pi)R_I \end{aligned} \quad (3)$$

In this context the polar coordinates ( $r, \theta$ ) are deemed the most appropriate, and Eq. (1) turns into  $d/dr[r(dV/dr)] \approx 0$ , via assuming the electroneutrality for the substantial bulk space of the interelectrode medium. Solving with the respective potentiostatic boundary condition of  $V(R_I) = V_I$ ,  $V(R_O) = V_O$  one gets

$$\begin{aligned} \hat{V} &= \frac{\ln(r) - \ln(R_I)}{\ln(R_O) - \ln(R_I)} \\ &= \frac{\ln(1 + 2\pi \hat{r})}{\ln(1 + 2\pi)}, \end{aligned} \quad (4)$$

where  $\hat{V} = V - V_-/V_+ - V_-$  is the dimensionless voltage normalized into the interelectrode potential and  $\hat{r} = r - R_I/R_O - R_I$  is the dimensionless radial measure normalized to the interelectrode distance. Thus,  $0 \leq \hat{r}, \hat{V} \leq 1$ . Respectively, the initial electric field  $E_r$  will be solely in the radial direction, merely due to initial azimuthal symmetry, and will be obtained as

$$\hat{E}_r = -\frac{2\pi}{\ln(1 + 2\pi)} \frac{1}{1 + 2\pi \hat{r}}, \quad (5)$$

where  $\hat{E} = E R_O - R_I/V_+ - V_-$  is the normalized electric field with respect to the equivalent planar arrangement.

Figures 2(a) and 2(b) describe the profiles for the initial electric potential  $\hat{V}$  and electric field  $\hat{E}$ , respectively, for various ratios of inner to outer radii  $R_I/R_O$ , which determines

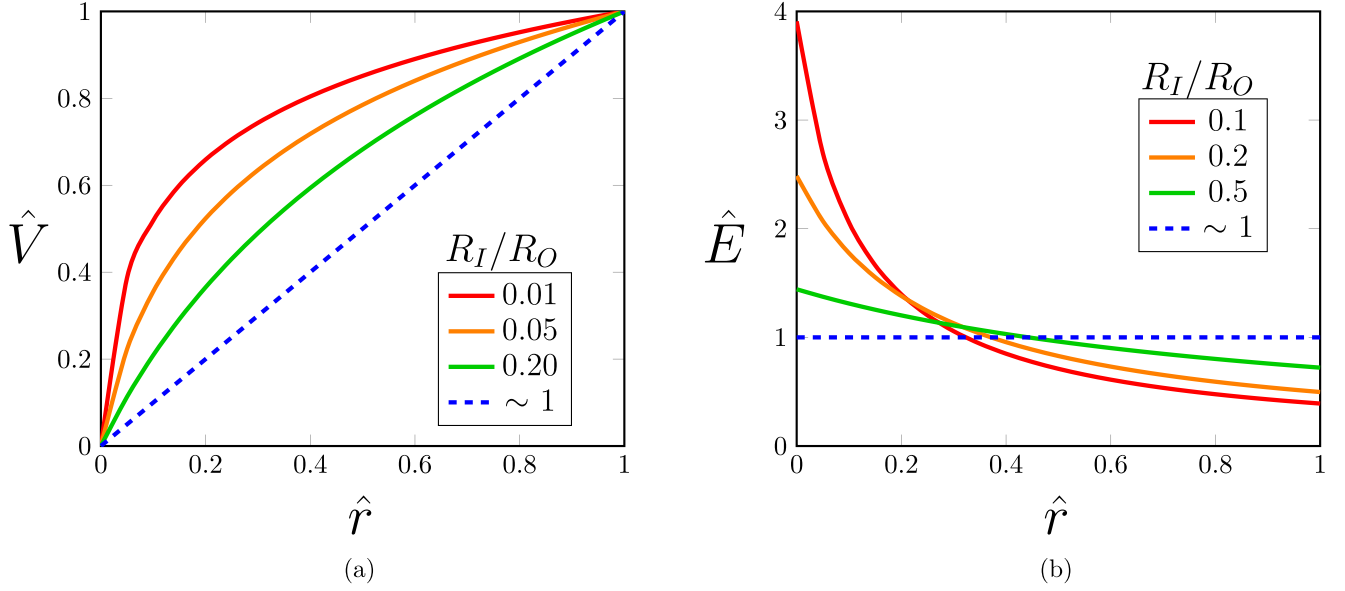


FIG. 2. Initial electric potential  $\hat{V}$  and electric field  $\hat{E}$  vs the radius ratio  $R_I/R_O$  (or curvature ratio  $\kappa_O/\kappa_I$ ). The extreme limit of  $R_I/R_O \rightarrow 1$  resembles the flat electrode arrangement. (a) Voltage  $\hat{V}$  profile versus the non-dimensional distance  $\hat{r}$  for various inner-to-outer radii ratio  $R_I/R_O$ . (b) Electric field variation  $\hat{E}$  versus the non-dimensional distance  $\hat{r}$  for various inner-to-outer radii ratio  $R_I/R_O$ .

the outstanding curvature. The distributions for the planar arrangement are also given by approximating when  $R_I \rightarrow R_O$ .

### B. Stochastic modeling

In order to extend the timescale of the simulations, we use the previously developed and verified coarse-grained modeling [34], which extrapolates the movements in the interatomic collisions and maps the average progress of the multitudes of interatomic collisions to a single move, as illustrated in Fig. 3, and significantly reduces the computational cost.

Such averaged electrochemical displacement is the result of the two distinct factors for ionic motion, where the former is the diffusion drive  $\delta \mathbf{r}_D$  from high-to-low concentration zones, employing mean-square displacement [37] as

$$\delta \mathbf{r}_D = \sqrt{2D\delta t} \hat{\mathbf{g}}, \quad (6)$$

where  $D$  is the diffusivity of the ions in the electrolytic solution and  $\hat{\mathbf{g}}$  is a random unit vector, representing the random (i.e., Brownian) motion. In fact, in the atomic scale ( $\sim \text{nm}$ ), the random unit vector  $\hat{\mathbf{g}}$  tends to uniformize the concentration map, where each ion with the collide-and-repel interaction during the random walks (i.e., Brownian dynamics) will gradually move from the higher to lower concentration zones after repetitive moves. The latter drive is due to the effect of the external electric field  $\mathbf{E}$  on the charge carriers, converging to a constant drift velocity of  $\mu \mathbf{E}$  after a short period of initial acceleration. Therefore, their electromigration displacement  $\delta \mathbf{r}_M$  in the same time interval  $\delta t$  would be

$$\delta \mathbf{r}_M = \mu \mathbf{E} \delta t. \quad (7)$$

Consequently, the total ionic displacement  $\delta \mathbf{r}$  is the sum of the aforementioned factors as

$$\delta \mathbf{r} = \delta \mathbf{r}_D + \delta \mathbf{r}_M, \quad (8)$$

which is visualized in Fig. 3. The simulation is performed for both planar [Fig. 1(a)] and polar [Fig. 1(b)] electrode arrangements, as follows:

1. Construct an initial electrode geometries with the presumed given voltage values.
2. Establish the initial electric field, which analytically is obtained in Eq. (5), and the planar case would be specific to  $\hat{r} \rightarrow 1$ .
3. Distribute the specified number of ions  $N$  randomly in the interelectrode space.
4. Let the ions move based on the displacement relationship given in Eq. (8) for the specified coarse time increment  $\delta t$ . For planar simulation of the scale  $l_{\text{SIM}}$ , the periodic boundary condition is applied, such that if an ion exits the boundary it automatically enters from the opposite side ( $x + l_{\text{SIM}}$  for exiting from left and  $x - l_{\text{SIM}}$  for exiting from the right). As well, for both planar and polar simulations, if an ion leaves the domain from the upper (outer) electrode, that move is canceled and the random motion is repeated until it falls within the interelectrode space. In this regard the polar move has been expressed in terms of the planar movements and reverted to the polar components. Hence, if  $(r_1, \theta_1)$  is the initial position of an ion, the next Cartesian position  $(x_2, y_2)$  after the time interval of  $\delta t$  is obtained as

$$\begin{aligned} x_2 &= r_1 \cos \theta_1 + \delta \mathbf{r}_{D,x} + \delta \mathbf{r}_{M,x} \\ y_2 &= r_1 \sin \theta_1 + \delta \mathbf{r}_{D,y} + \delta \mathbf{r}_{M,y} \end{aligned},$$

where the  $\square_x$  and  $\square_y$  notions represent the  $x$  and  $y$  components of the respective displacements. Subsequently, the polar form of the position at the end of time increment  $\delta t$  would be

$$\begin{aligned} r_2 &= \sqrt{x_2^2 + y_2^2} \\ \theta_2 &= \tan^{-1} \left( \frac{y_2}{x_2} \right), \end{aligned}$$

where  $0 \leq \theta_2 \leq 2\pi$ .

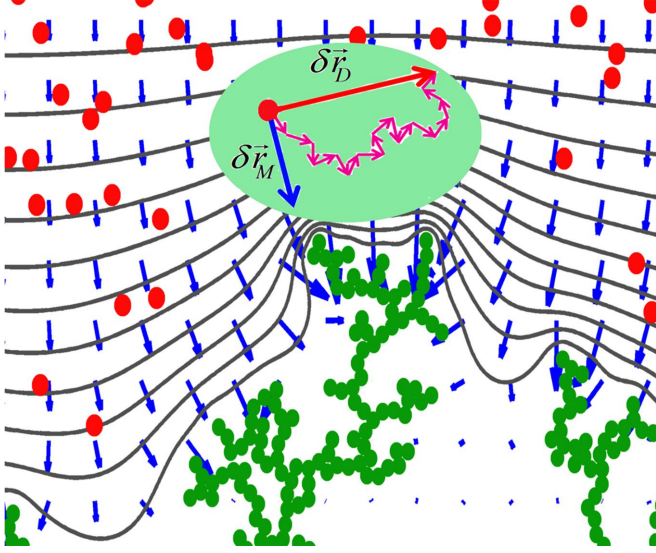


FIG. 3. Schematics of the coarse-grained modeling for dendritic evolution, illustrating the diffusional  $\delta \vec{r}_D$  (red) and migrational  $\delta \vec{r}_M$  (blue) displacements. The coarse-grained model combines the average of multitudes of smaller-scale diffusion moves, shown as pink vectors, in one single move. Red circles: Free ions, green branches: Dendrites, blue vectors: Electric field, gray lines: Electric potential contours. Reprinted with permission from Ref. [35], copyright 2019 American Physical Society.

5. After the movement, if there is an overlap with an ion to the bottom (inner) electrode or anywhere in the body of the dendrite atoms, it is attached in the interspecified interatomic distance from the overlapping position. Such a condition could be expressed as

$$|\mathbf{r}_{ION,i} - \mathbf{r}_{DND,j}| \leq d_{\text{Bond}},$$

where  $\mathbf{r}_{ION,i}$  and  $\mathbf{r}_{DND,i}$  are the position of the moving ion  $i$  and overlapping dendrite atom  $j$ , respectively, and  $d_{\text{Bond}}$  is interatomic bond distance. The probability of reaction  $p$  upon overlap is a material-dependent property, which correlates with the rate of electron transfer  $k_{ET}$  obtained from Marcus's theory [38] and is broken down to several parameters [39]. For simplicity and focus on the geometric differences between planar and polar frameworks it has been assumed to be unity ( $p = 1$ ), which means that the ion turns dendritic immediately upon getting close enough to the dendritic structure.

Subsequently a replacement ion is released from the counter-electrode in a random position on its surface (i.e.,  $r_{ION} = R_O$ ,  $0 \leq \theta_{ION} \leq 2\pi$ ) to maintain the constant number of free ions  $N$ . In this case, since the growing dendrite is physically connected to the electrode, it will carry the same potential, which provides a third boundary condition for solving Eq. (1), as  $V_{\text{DEND}} = V_-$  and the real-time electric field is recalculated. Meanwhile, the electroneutrality is assumed ( $\rho \approx 0$ ), leaving the variation in the voltage and electric field distributions solely due to changes in the geometry of the growing dendritic branches.

In real-time computation the potential is achieved through solving the following Laplacian relationship for the polar co-

ordinates:

$$\nabla^2 V = \frac{d^2 V}{dr^2} + \frac{1}{r} \frac{dV}{dr} + \frac{1}{r^2} \frac{d^2 V}{d\theta^2}, \quad (9)$$

where the range of parameters is  $R_I \leq r \leq R_O$  and  $0 \leq \theta \leq 2\pi$ . Adopting the finite difference scheme we divide the domain into the radial  $\delta r$  and azimuthal  $\delta \theta$ . Hence  $V_{i,j}$  represents the potential in the radial distance  $r_i$  and azimuthal orientation of  $\theta_j$ , and Eq. (9) gets simplified into

$$\frac{V_{i+1,j} - 2V_{i,j} + V_{i-1,j}}{\delta r^2} + \frac{1}{r_i} \frac{V_{i+1,j} - V_{i,j}}{\delta r} + \frac{1}{r_i^2} \frac{V_{i,j+1} - 2V_{i,j} + V_{i,j-1}}{\delta \theta^2} \approx 0,$$

where  $\delta r$  and  $\delta \theta$  are the length of segmentations in their respective directions. Rearranging versus the neighbor values one gets

$$V_{i,j} = Q_1 V_{i+1,j} + Q_2 V_{i-1,j} + Q_3 V_{i,j+1} + Q_4 V_{i,j-1},$$

where the  $Q_i$  are the quotients obtained as

$$Q_1 = \frac{r_i \delta \theta^2}{A} (r_i + \delta r), \quad Q_2 = \frac{r_i^2 \delta \theta^2}{A}, \quad Q_3 = Q_4 = \frac{\delta r^2}{A}$$

and  $A$  is an areal coefficient attained as  $A = 2r_i^2 \delta \theta^2 + r_i \delta r \delta \theta^2 + 2\delta r^2$ . The boundary conditions are updated in every iteration, and consequently the electric field vectors  $E_{i,j}^r$  and  $E_{i,j}^\theta$  are obtained via the finite difference method as

$$E_{i,j}^r = -\frac{V_{i+1,j} - V_{i,j}}{\delta r}, \quad E_{i,j}^\theta = -\frac{1}{r_i} \frac{V_{i,j+1} - V_{i,j}}{\delta \theta}.$$

6. The simulation is stopped either when the number of atoms in the dendrite reaches the prescribed value of  $N$  or the growing dendrite has reached the counter-electrode.

### C. Density computations

In order to address the morphological aspects of the electrodeposits, two distinctive measures have been defined and tracked throughout the simulation. The first measure  $\hat{h}$  represents the maximum reach of the electrodeposits. Hence, normalizing to the maximum value for planar and polar coordinates yields

$$\hat{h}_{xy} = \frac{y_{\text{max}}}{l}, \quad \hat{h}_{r\theta} = \frac{r_{\text{max}} - R_I}{R_O - R_I},$$

where  $0 \leq \hat{h}_{xy}, \hat{h}_{r\theta} \leq 1$  and  $y_{\text{max}}$  and  $r_{\text{max}}$  represent the maximum height and radial distance of the dendrite in the planar and polar configurations, respectively. The second measure is the density  $\rho$ , which represents the packedness of the crystals and is defined spatially by the filling-to-total areal ratio. For the rectangular domain defined with the scale of  $l = 2\pi R_I$  [Eq. (3)], the density  $\rho_{xy}$  would be

$$\rho_{xy} = \frac{n\pi a^2}{l^2} \frac{1}{\hat{h}_{xy}},$$

where  $n$  is the real-time number of deposited atoms. Respectively for the polar electrodeposition, one gets the density  $\rho_{r\theta}$

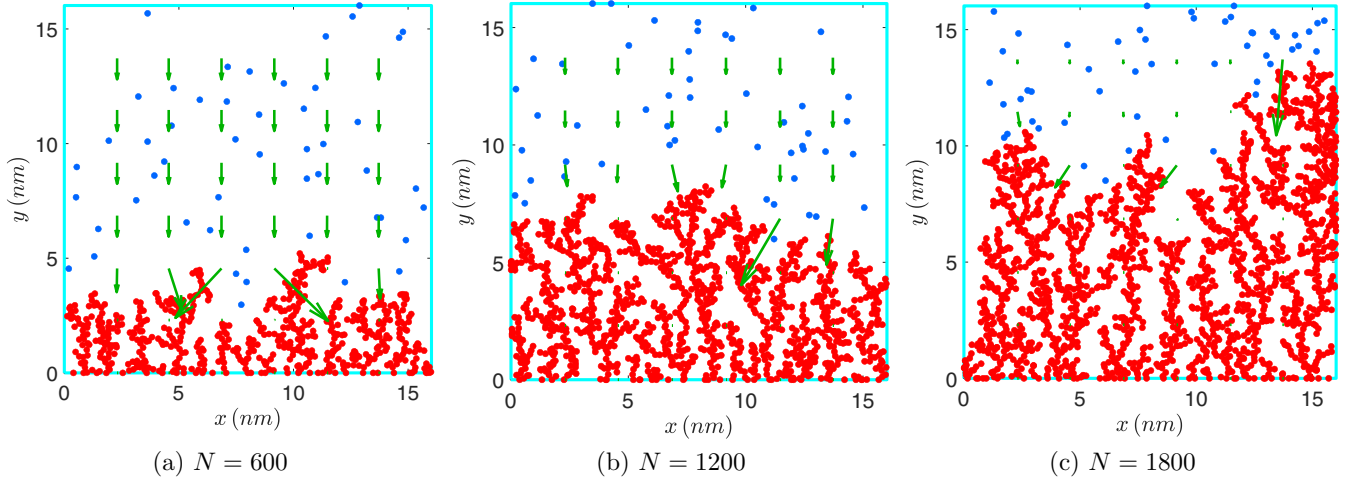


FIG. 4. Planar dendrite morphologies grown vs the number of deposited atoms  $N$ . Red: Dendrites, blue: Free ions, green: Electric field vectors.

as

$$\rho_{r\theta} = \frac{na^2}{4\pi R_I^2} \frac{1}{\hat{h}_{r\theta}(1 + \pi \hat{h}_{r\theta})};$$

therefore the relationships are inverse for the planar arrangement and nonlinearly opposite correlation for the polar configuration.

Figures 4 and 5 show sample-grown morphologies of the dendrites for the specified number of deposited atoms  $N$ , based on the simulation parameters presented in Table I. Meanwhile, the mobility  $\mu$  is simply obtained from the Einstein relationship as [43]

$$\mu = \frac{De}{k_B T}. \quad (10)$$

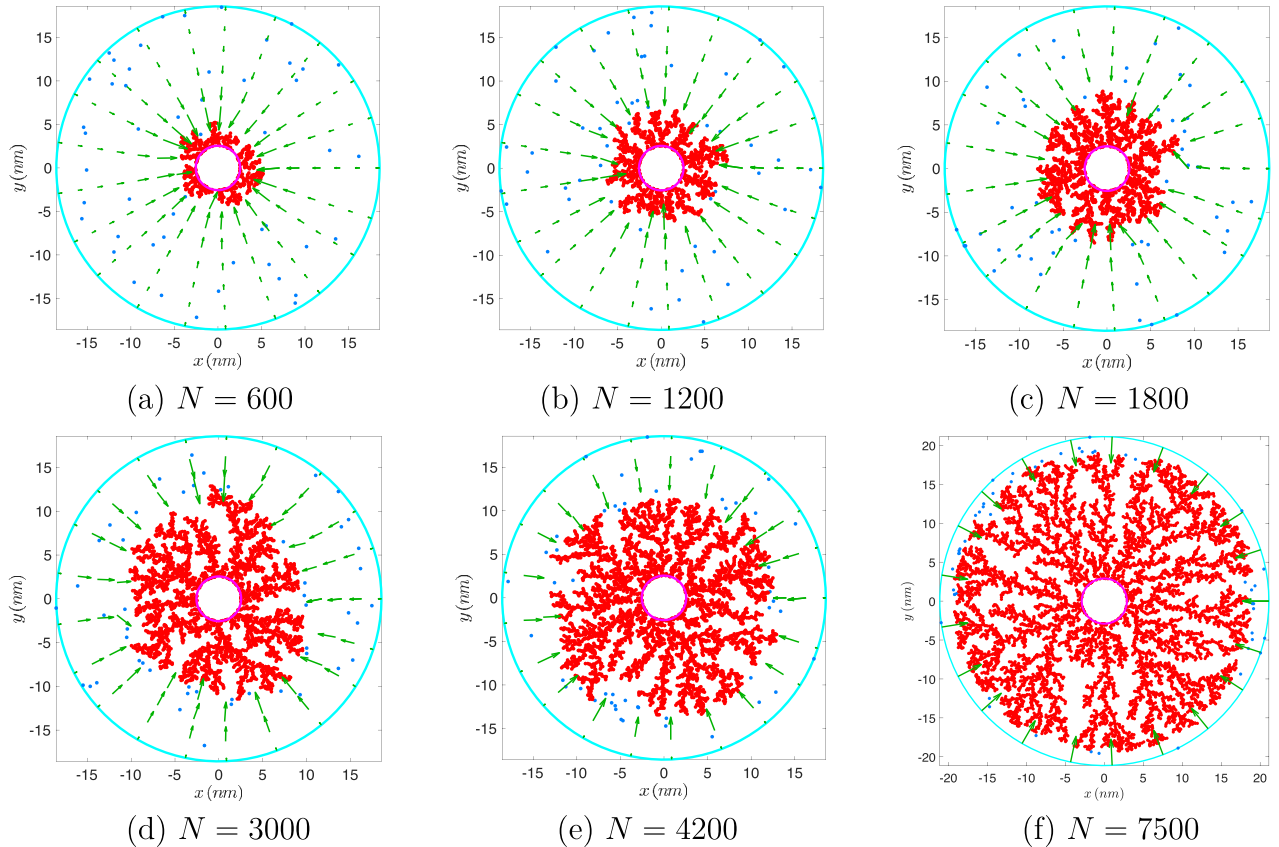


FIG. 5. Dendrite morphologies are grown on the curved surface vs the number of deposited atoms  $N$ . Red: Dendrites, blue: Free ions, green: Electric field vectors.



TABLE I. Simulation parameters.

Parameter	Value	Unit	Ref.	Constant	Value	Unit	Ref.
$D$	$2.58 \times 10^{-10}$	$\text{m}^2 \text{s}^{-1}$	[35]	$N_{\text{Planar}}$	$\{600, \dots, 1800\}$	[ ]	Assumed
$e$	$1.6 \times 10^{-19}$	C	[40]	$N_{\text{Polar}}$	$\{600, \dots, 7500\}$	[ ]	Assumed
$k_B$	$1.38 \times 10^{-23}$	$\text{J K}^{-1}$	[40]	$l$	$130a$	$\text{\AA}$	Assumed
$T$	298	K	[41]	$R_l$	29	$\text{\AA}$	Eq. (3)
$d_{\text{Bond}}$	$2a$	$\text{\AA}$	[42]	$R_o$	186	$\text{\AA}$	Eq. (3)
$a$	1.45	$\text{\AA}$	[42]	$\mu$	$10^{-8}$	$\text{m}^2 \text{V}^{-1} \text{s}^{-1}$	Eq. (10)
$\hat{V}_+$	1	[ ]	Normalized	$\delta r$	0.18	nm	Assumed
$\hat{V}_-$	0	[ ]	Normalized	$\delta t$	0.1	ns	Assumed

As well, the densities  $\rho_{xy}$ ,  $\rho_{r\theta}$  and the maximum dendrite reach  $\hat{h}_{xy}$ ,  $\hat{h}_{r\theta}$  are tracked in real time and visualized in Fig. 6.

### III. RESULTS AND DISCUSSION

Analyzing the effective terms for the ionic flux, represented in Eqs. (6) and (7), one notices that while the diffusion term tends to average out the ionic distribution (i.e., *favorable*), the electromigration term tends to direct the ions in specific directions and grow branches (i.e., *unfavorable*). In such a trade-off one could define a measure for dendricity  $\lambda$  as the ratio of their respective movements, which is simplified into

$$\lambda = \frac{\delta \mathbf{r}_M}{\delta \mathbf{r}_D} = \frac{e}{k_B T} \sqrt{\frac{D \delta t}{2}} E.$$

In order to compare the polar arrangement with the planar version we define the notion of their ratio as  $\hat{\lambda} = \square_{\text{Polar}} / \square_{\text{Planar}}$ . Hence considering the equivalent definitions in Sec. II A one gets the dendricity ratio  $\hat{\lambda}$  as

$$\hat{\lambda} = \hat{E}.$$

In particular, for the initiation state, one has

$$\hat{\lambda} = \frac{2\pi}{\ln(1+2\pi)} \frac{1}{1+2\pi\hat{r}},$$

which from Fig. 2(b) means that the dendritic tendency of the polar configuration is higher than the planar version during the initiation growth, and lower in the later stages of the

propagation. In fact, for the curved interface, the microstructures initially grow faster (i.e., *disadvantageous*), and in return, during the later stages they build up at a slower pace (i.e., *advantageous*) than the planar electrodes. Such a naturally formed electric profile merely due to the electrode curvature is commensurate with the form of optimized charging for the extreme inhibition of the dendrites [44], which, in the trade-off, ultimately forms a more packed microstructure during the entire charging period, as shown in Fig. 6 for a multiple number of deposited atoms  $N$ . Meanwhile the location of  $|E_{xy}| = |E_{r\theta}|$  would be

$$\hat{r} = \frac{1}{\ln(1+2\pi)} - \frac{1}{2\pi} \approx 0.34,$$

which represents the radial distance, where the growth rate of both planar and equivalent polar rates is identical. As well, the oscillatory behavior in the evolution of the density versus the dendritic build up is due to random placement of the upcoming ions within the microstructure, where any connecting ion to another periphery reduces the density, whereas any infiltrating ion to the inner voids increases the respective density.

Considering the scholastic nature of the dendritic evolution, the morphologies obtained from the planar and polar arrangements, shown in Figs. 4 and 5, one notices that on average the polar arrangement lasts substantially longer both in terms of number of atoms and the time duration before the short circuit. Considering the values given in Table I, the respective ratios of  $\hat{N}_{\text{Short}}$  and  $\hat{t}_{\text{Short}}$  are obtained from four simulations to obtain more confidence in the analogy, with

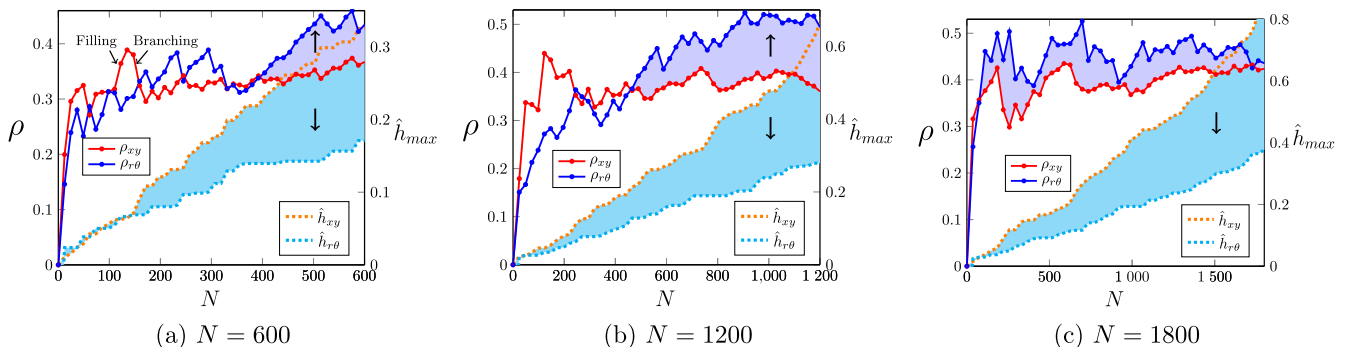


FIG. 6. Tracking of the microstructure densities  $\rho_{xy}$ ,  $\rho_{r\theta}$  and the maximum reach measure  $\hat{h}_{xy}$ ,  $\hat{h}_{r\theta}$  vs the number of electrodeposited atoms for the planar and polar electrode configurations.

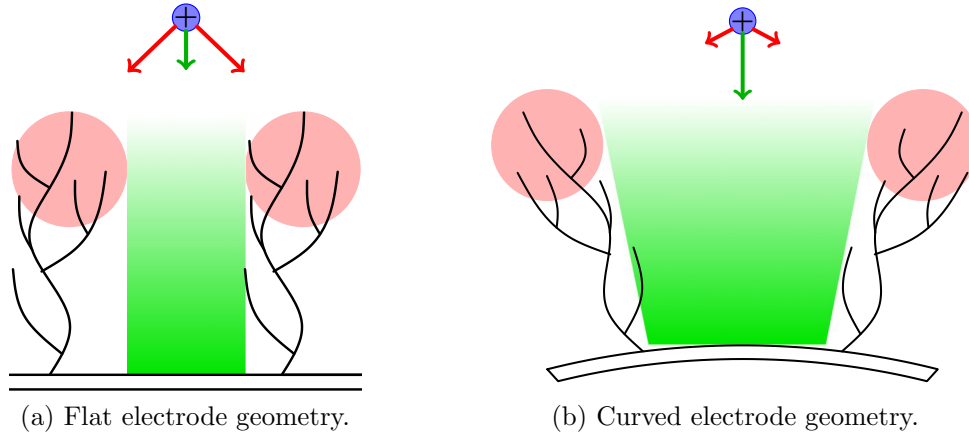


FIG. 7. Schematics of the feasibility of the pathway for the electrodepositing ion (blue), when exposed to planar (a) vs the curved (b) geometry of the electrodes. The tendency of the movement is shown by the red and green vectors, which are toward the peak of the dendrites (highlighted red) vs the inner regions (highlighted green). As shown, the curved geometry provides more openness for the formation of packed microstructures.

identical initial parameters as

$$\begin{aligned}\hat{N}_{\text{Short}} &= 3.85 \pm 0.28 \\ \hat{t}_{\text{Short}} &= 3.81 \pm 0.14\end{aligned}$$

As well, the ratio of the average current before the short circuit  $\hat{I}$  is obtained as

$$\hat{I} = \frac{\hat{N}_{\text{Short}}}{\hat{t}_{\text{Short}}} \approx 1.$$

Meanwhile, the ratio of the average electric field  $\hat{E}$  is additionally obtained as

$$\hat{E} = \int_0^1 \frac{2\pi}{\ln(1+2\pi)} \frac{1}{1+2\pi\hat{r}} d\hat{r} = 1,$$

which infers as the direct correlation between the average current density  $\hat{I}$  and the electric field  $\hat{E}$ . Such a direct correlation is especially evident in the beginning of the charging process since the concentration is uniform and the sole drive for the ionic motion is the electromigration from the externally imposed electric field  $E$ . As well, it additionally becomes obvious for the case of dilute concentrations ( $C \downarrow$ ) and high-power applications ( $E \uparrow$ ). In this regard, the dominance of the electromigration term over the diffusion has been recently illustrated [45], which proves the hypothesis above.

In addition to tuning of the electric field in favor of the polar electrode that was explained earlier, another factor would be the concentration. Comparing the areas of the planar and analogous polar electrode arrangement one gets

$$\frac{A_{\text{Polar}}}{A_{\text{Planar}}} = \pi + 1 \approx 4.14,$$

which implies the inverse ratio for the average concentration, as  $\bar{C}_{\text{Polar}} \sim 1/4\bar{C}_{\text{Planar}}$ , and the respective electrodeposition will occur more smoothly.

Geometry-wise, the advantage of the curved electrode is that the the larger counter-electrode has a higher dispersion (less concentration) of ions, and the growing microstructures have more distancing in the outer regions as shown in Fig. 7.

Hence, the upcoming ions initially face larger branch separation and get more of a chance to move inside and form a packed structure. In fact, for the polar arrangement, we take advantage that during the later stage of the dendritic growth there is a larger opening due to larger radius.

Since both planar and polar frameworks carry identical electrolyte and diffusivity  $D$ , the diffusion terms get canceled out for obtaining the dendricity ratio  $\hat{\lambda}$ . However, it is important to note that the electrodeposition is the consequence of the ionic transport within the electrolyte (i.e., diffusion) and, later, the ionic reduction upon reaching the electrode surface (i.e., reaction). Since such diffusion-reaction dynamics occurs in series order, the event of the smaller pace will be controlling the total effective flux  $J$  of electrodeposition. Hence, the respective comparison between the polar and planar configurations assumes the abundance of the ions in the immediate vicinity of the dendrite interface, which typically occurs during the initial stages of the charging as well as the prolonged charging for the underlimiting currents ( $J < J^*$  and  $J^*$  is the current of ionic exhaust in the electrodeposition where  $C \rightarrow 0$ ) [46]. However, during the extreme currents where the ions are exhausted on the electrode surface ( $J > J^*$ ), the feeding rate from the bulk solution becomes deterministic, and the diffusivity of the electrolytic medium  $D$  becomes the controlling factor for electrodeposition rate.

Needless to mention, assuming unity for the probability of reaction ( $p = 1$ ) ultimately generates more pronounced dendrites, and obtaining the material-dependent smaller probability values will still leave the polar arrangement more advantageous than the planar version ( $\rho_{\text{Polar}} > \rho_{\text{Planar}}$ ,  $\hat{h} < 1$ ,  $\hat{N}_{\text{Short}} > 1$ ), albeit with a different ratios. As well, for the case scenarios of the lower curvature, where the interface radius turns indefinitely large ( $R_I \gg l$ ), the planar and equivalent domains will turn to a thin strip ( $W \gg l$ ) and thin ring ( $R_I \approx R_O$ ), where the effect of the curvature will become negligible and packing densities will become similar. However, for the square planar arrangement ( $W \approx l$ ), the periodic boundary condition extends the results for case scenario aspect ratio ( $R_I \gg l$ ) leading to identical packing density.

Finally, the density calculation  $\rho$  for this study, which inversely correlates with the dendricity  $\lambda$ , has been defined as the occupied fraction of the domain by the atoms. As well, other measures could be utilized in this regard, such as the average coordination number, orientation of branches, and tortuosity of the growing interface [47]. The higher average coordination number infers that each individual atom accommodates more neighbors leading to a more packed structure and vice versa. As well, the more directed growth with similar branch orientation signifies more ordered pattern, while the inhomogeneous growth with random branching could mostly occupy the space and ultimately could reduce the growing density.

#### IV. CONCLUSION

In this paper we have developed a comparative framework for the dendritic evolution in the the analogous polar (i.e., circular) electrode arrangement versus the planar version. Subsequently, we have compared their tendency for branching in the various stages of the dendritic development via

analytical obtaining of the initial curvature-dependent electric field distribution. Consequently, we have adopted the coarse-grained modeling, which works based on the extended scales of time and space ( $\sim\mu\text{s}$ ,  $\sim\text{nm}$ ) than on the typical interatomic collisions ( $\sim\text{fs}$ ,  $\sim\text{\AA}$ ), where the reduction in the growth measure enhancement in the formed density in the cylindrical cell versus the planar cell is quantified. The obtained characterization could be useful as a simple and versatile tool for dendrite-resilient electrode design, particularly in high-power applications.

The raw data for producing the results in this paper are freely available upon request from the corresponding author.

#### ACKNOWLEDGMENT

A.T. thanks the Masri Institute at American University of Beirut for support, Grant Award No. 103919.

The authors declare that they have no competing financial interests to influence the work reported in this paper.

- 
- [1] I. Hadjipaschalis, A. Poulidakis, and V. Efthimiou, Overview of current and future energy storage technologies for electric power applications, *Renew. Sustain. Energy Rev.* **13**, 1513 (2009).
  - [2] G.-A. Nazri and G. Pistoia, *Lithium Batteries: Science and Technology* (Springer Science & Business Media, New York, NY, 2008).
  - [3] Y. Wang, B. Liu, Q. Li, S. Cartmell, S. Ferrara, Z. D. Deng, and J. Xiao, Lithium and lithium ion batteries for applications in microelectronic devices: A review, *J. Power Sources* **286**, 330 (2015).
  - [4] M. S. Whittingham, History, evolution, and future status of energy storage, *Proc. IEEE* **100**, 1518 (2012).
  - [5] U. Shahzad, The need for renewable energy sources, *Energy* **2**, 16 (2012).
  - [6] T. Kim, W. Song, D.-Y. Son, L. K. Ono, and Y. Qi, Lithium-ion batteries: Outlook on present, future, and hybridized technologies, *J. Mater. Chem. A* **7**, 2942 (2019).
  - [7] R. Van Noorden, The rechargeable revolution: A better battery, *Nature (London)* **507**, 26 (2014).
  - [8] K. H. LaCommare and J. H. Eto, *Understanding the Cost of Power Interruptions to us Electricity Consumers*, Technical Report No. LBNL-55718 (Lawrence Berkeley National Laboratory (LBNL), Berkeley, California, 2004).
  - [9] M. Kaliaperumal, M. S. Dharanendrakumar, S. Prasanna, K. V. Abhishek, R. K. Chidambaram, S. Adams, K. Zaghib, and M. V. Reddy, Cause and mitigation of lithium-ion battery failure: A review, *Materials* **14**, 5676 (2021).
  - [10] M. Balaish, A. Kraytsberg, and Y. Ein-Eli, A critical review on lithium–air battery electrolytes, *Phys. Chem. Chem. Phys.* **16**, 2801 (2014).
  - [11] S.-E. Sheng, L. Sheng, L. Wang, N. Piao, and X. He, Thickness variation of lithium metal anode with cycling, *J. Power Sources* **476**, 228749 (2020).
  - [12] K. Amine, I. Belharouak, Z. Chen, T. Tran, H. Yumoto, N. Ota, S.-T. Myung, and Y.-K. Sun, Nanostructured anode material for high-power battery system in electric vehicles, *Adv. Mater.* **22**, 3052 (2010).
  - [13] F. Orsini, A. D. Pasquier, B. Beaudoin, and J. M. Tarascon, *In situ* scanning electron microscopy (SEM) observation of interfaces with plastic lithium batteries, *J. Power Sources* **76**, 19 (1998).
  - [14] C. Brissot, M. Rosso, J. N. Chazalviel, and S. Lascaud, Dendritic growth mechanisms in lithium/polymer cells, *J. Power Sources* **81–82**, 925 (1999).
  - [15] C. Brissot, M. Rosso, J. N. Chazalviel, P. Baudry, and S. Lascaud, *In situ* study of dendritic growth in lithium/PEO-salt/lithium cells, *Electrochim. Acta* **43**, 1569 (1998).
  - [16] K. Xu, Nonaqueous liquid electrolytes for lithium-based rechargeable batteries, *Chem. Rev.* **104**, 4303 (2004).
  - [17] C. P. Nielsen and H. Bruus, Morphological instability during steady electrodeposition at overlimiting currents, *Phys. Rev. E* **92**, 052310 (2015).
  - [18] P. P. Natsiavas, K. Weinberg, D. Rosato, and M. Ortiz, Effect of prestress on the stability of electrode–electrolyte interfaces during charging in lithium batteries, *J. Mech. Phys. Solids* **95**, 92 (2016).
  - [19] J. Steiger, D. Kramer, and R. Monig, Mechanisms of dendritic growth investigated by *in situ* light microscopy during electrodeposition and dissolution of lithium, *J. Power Sources* **261**, 112 (2014).
  - [20] H. Liu, X.-B. Cheng, J.-Q. Huang, H. Yuan, Y. Lu, C. Yan, G.-L. Zhu, R. Xu, C.-Z. Zhao, L.-P. Hou *et al.*, Controlling dendrite growth in solid-state electrolytes, *ACS Energy Lett.* **5**, 833 (2020).
  - [21] C.-Z. Zhao, H. Duan, J.-Q. Huang, J. Zhang, Q. Zhang, Y.-G. Guo, and L.-J. Wan, Designing solid-state interfaces on lithium-metal anodes: A review, *Sci. China Chem.* **62**, 1286 (2019).
  - [22] T. Foroozan, F. A. Soto, V. Yurkiv, S. Sharifi-Asl, R. Deivanayagam, Z. Huang, R. Rojaee, F. Mashayek, P. B. Balbuena, and R. Shahbazian-Yassar, Synergistic effect of



- graphene oxide for impeding the dendritic plating of Li, *Adv. Funct. Mater.* **28**, 1705917 (2018).
- [23] K. Shen, Z. Wang, X. Bi, Y. Ying, D. Zhang, C. Jin, G. Hou, H. Cao, L. Wu, G. Zheng *et al.*, Magnetic field-suppressed lithium dendrite growth for stable lithium-metal batteries, *Adv. Energy Mater.* **9**, 1900260 (2019).
- [24] Y. Ren, Y. Zhou, and Y. Cao, Inhibit of lithium dendrite growth in solid composite electrolyte by phase-field modeling, *J. Phys. Chem. C* **124**, 12195 (2020).
- [25] A. Jana, D. R. Ely, and R. E. García, Dendrite-separator interactions in lithium-based batteries, *J. Power Sources* **275**, 912 (2015).
- [26] L. Holzer, D. Wiedenmann, B. Münch, L. Keller, M. Prestat, P. Gasser, I. Robertson, and B. Grobéty, The influence of constrictivity on the effective transport properties of porous layers in electrolysis and fuel cells, *J. Mater. Sci.* **48**, 2934 (2013).
- [27] K. Rafiz, D. R. L. Murali, and J. Y. S. Lin, Suppressing lithium dendrite growth on lithium-ion/metal batteries by a tortuously porous  $\gamma$ -alumina separator, *Electrochim. Acta* **421**, 140478 (2022).
- [28] I. V. Thorat, D. E. Stephenson, N. A. Zacharias, K. Zaghib, J. N. Harb, and D. R. Wheeler, Quantifying tortuosity in porous Li-ion battery materials, *J. Power Sources* **188**, 592 (2009).
- [29] A. Cannon and E. M. Ryan, Characterizing the microstructure of separators in lithium batteries and their effects on dendritic growth, *ACS Appl. Energy Mater.* **4**, 7848 (2021).
- [30] C. Yuan, W. Lu, and J. Xu, Unlocking the electrochemical-mechanical coupling behaviors of dendrite growth and crack propagation in all-solid-state batteries, *Adv. Energy Mater.* **11**, 2101807 (2021).
- [31] C. Monroe and J. Newman, The effect of interfacial deformation on electrodeposition kinetics, *J. Electrochem. Soc.* **151**, A880 (2004).
- [32] D. A. Cogswell, Quantitative phase-field modeling of dendritic electrodeposition, *Phys. Rev. E* **92**, 011301(R) (2015).
- [33] C.-H. Chen and C.-W. Pao, Phase-field study of dendritic morphology in lithium metal batteries, *J. Power Sources* **484**, 229203 (2021).
- [34] A. Aryanfar III, D. Brooks, B. V. Merinov, W. A. Goddard III, A. J. Colussi, and M. R. Hoffmann, Dynamics of lithium dendrite growth and inhibition: Pulse charging experiments and Monte Carlo calculations, *J. Phys. Chem. Lett.* **5**, 1721 (2014).
- [35] A. Aryanfar, M. R. Hoffmann, and W. A. Goddard III, Finite-pulse waves for efficient suppression of evolving mesoscale dendrites in rechargeable batteries, *Phys. Rev. E* **100**, 042801 (2019).
- [36] D. Halliday, R. Resnick, and J. Walker, *Fundamentals of physics* (John Wiley & Sons, 2013).
- [37] J. Philibert, One and a half century of diffusion: Fick, Einstein, before and beyond, *Diffusion Fund.* **4**, 6.1 (2006).
- [38] R. A. Marcus and N. Sutin, Electron transfers in chemistry and biology, *Biochim. Biophys. Acta, Rev. Bioenerg.* **811**, 265 (1985).
- [39] A. Aryanfar, S. Medlej, and W. A. Goddard III, Morphometry of dendritic materials in rechargeable batteries, *J. Power Sources* **481**, 228914 (2021).
- [40] D. B. Newell and E. Tiesinga, The international system of units (SI), NIST Spec. Publ. **330**, 1 (2019).
- [41] B. N. Taylor and E. R. Cohen, Recommended values of the fundamental physical constants: A status report, *J. Res. Natl. Ins. Stand. Technol.* **95**, 497 (1990).
- [42] J. C. Slater, Atomic radii in crystals, *J. Chem. Phys.* **41**, 3199 (1964).
- [43] K. Dill and S. Bromberg, *Molecular Driving Forces: Statistical Thermodynamics in Biology, Chemistry, Physics, and Nanoscience* (Garland Science, 2010).
- [44] A. Aryanfar III, Y. Ghamlouche, and W. A. Goddard, Optimization of charge curve for the extreme inhibition of growing microstructures during electrodeposition, *MRS Bull.* **47**, 665 (2022).
- [45] A. Aryanfar, Linearized tracking of dendritic evolution in rechargeable batteries, *J. Electrochem. Soc.* **169**, 112507 (2022).
- [46] M. Rosso, Electrodeposition from a binary electrolyte: New developments and applications, *Electrochim. Acta* **53**, 250 (2007).
- [47] T. Dhara, A. Aryanfar, A. Ghosh, U. Ghosh, P. Mukherjee, and S. DasGupta, The role of pulse duty cycle and frequency on dendritic compression, *J. Phys. Chem. C* **127**, 4407 (2023).